Journal of Materials Chemistry A

ROYAL SOCIETY OF CHEMISTRY

PAPER

View Article Online
View Journal

Cite this: DOI: 10.1039/d5ta03421c

Microstructure-informed performance boost in solid oxide fuel cells through multiphysical modeling and machine learning

Li Duan, Zilin Yan,* Zehua Pan and Zheng Zhong*

The optimization of the macro- and microstructures of traditional solid oxide fuel cells (SOFCs) faces the dual challenges of time-consuming experimental iterations and insufficient exploration of parameter space. This study proposes an anode-supported SOFC optimization approach based on multiphysical modeling and machine learning, aiming to achieve the coordinated optimization design of its macro- and microstructures, thereby ensuring the improvement of power density and the reduction of failure probability. The study first constructed a database of maximum power density and failure probability based on multiphysical modeling, and then screened out 10 key features that affect the above two target parameters through feature engineering. On this basis, 15 machine learning predictive models were constructed, among which the random forest (RF) regression model showed excellent prediction performance, and the determination coefficients (R^2) of the maximum power density and failure probability predictive models reached 0.99 and 0.95 respectively. The cooperation of the genetic algorithm and RF obtained the optimal combination of key parameters, ensuring that the cell achieved the highest power output within the failure probability range of 0.632. The SOFC button cell prepared based on the cathode optimization results was experimentally verified, and its maximum power density reached 1.43 W cm^{-2}, which was 29% higher than the initial sample, verifying the effectiveness of the proposed optimization approach. In addition, Shapley additive explanations (SHAP) were introduced to improve the interpretability of the model. The results show that most key features have opposite effects on the two target quantities, demonstrating the necessity of considering the failure probability.

Received 30th April 2025
Accepted 28th July 2025

DOI: 10.1039/d5ta03421c

rsc.li/materials-a

1. Introduction

Solid oxide fuel cells (SOFCs), renowned for their high electrical efficiency and long-term stability,[1,2] are being widely adopted across residential power generation, industrial manufacturing, military applications, and more, positioning them as a forward-looking solution in renewable energy.[3–6] SOFCs consist of an anode, a cathode and an electrolyte, and operate based on the conduction of electrons (or electron holes) and the transport of oxide ions.[7] Based on their structure, SOFCs can be classified into three main types: electrolyte-supported SOFCs (ES-SOFCs), anode-supported SOFCs (AS-SOFCs), and metal-supported SOFCs (MS-SOFCs).[8,9] Among these, AS-SOFCs are more prevalent in commercial applications due to their higher power densities.[10,11] At the current stage, commercial AS-SOFCs typically employ porous nickel/yttria-stabilized zirconia (Ni/YSZ) as the composite anode, dense 8 mol% yttria-stabilized zirconia (8YSZ) as the electrolyte layer, gadolinium-doped cerium oxide (GDC) as the barrier layer, and porous lanthanum strontium cobalt ferrite (LSCF) as the cathode layer.[12]

The performance of an SOFC is heavily influenced by its macroscopic and microscopic structures, including electrode thickness, porosity, and phase composition (*e.g.*, Ni/YSZ volume ratio in cermet anodes).[13,14] These structural parameters directly impact key processes within the cell, such as mass transfer, heat transfer, and electrochemical reactions, ultimately determining the cell's output power, efficiency, and stability.[15,16] Among these, the maximum power density (P_{max}) and failure probability (P_f) are selected as critical metrics because they play a vital role in evaluating the actual performance and reliability of SOFC full cells.[17–20] As a result, optimizing the macroscopic and microscopic structures of SOFCs is essential for enhancing performance, reducing costs, and extending their lifespan.[21]

The optimization of SOFCs dates back to 1996, when Kleitz and Petitbon enhanced SOFC performance by refining electrode designs through an analysis of double-layer microstructures.[22] Costamagna *et al.* used analytical models to study the interaction between structural parameters (such as electrode thickness and porosity) and their impact on SOFC performance.[23] Bhattacharyya *et al.* developed an isothermal model to evaluate the performance of tubular SOFCs, demonstrating that optimizing factors such as anode thickness, porosity, and operating conditions can substantially enhance SOFC efficiency and

School of Science, Harbin Institute of Technology (Shenzhen), Shenzhen, 518055, China. E-mail: yanzilin@hit.edu.cn; zhongzheng@hit.edu.cn

overall performance.[24] Feng *et al.* used the finite element method (FEM) to determine the optimal geometric configuration to significantly improve the output power of tubular SOFCs, including the optimal anode, cathode and electrolyte thicknesses and the optimal cell length.[25] Abdullah and Liu investigated simulation-based methods to optimize the microstructure of SOFCs for low-temperature operation, demonstrating that tailoring electrode microstructures can significantly improve power output and efficiency, enabling effective performance at reduced operating temperatures.[26] Goncalves introduced a novel numerical framework that combines two-dimensional (2D) topology optimization with three-dimensional (3D) multiphysical modeling to optimize SOFC channel layouts.[27] This method enhanced SOFC performance by achieving more uniform flow and current density distributions, reducing pressure drops, and improving overall system efficiency and durability.

In addition to the numerical calculation methods introduced above, there are also many studies focusing on experimental optimization.[28–32] Haanappel *et al.* investigated the optimization of processing and microstructural parameters of LSM cathodes to enhance the electrochemical performance of AS-SOFCs.[28] They achieved a current density of 1.4 A cm^{-2} by adjusting the thickness of the LSM/YSZ cathode and the cathode current collection layer. Ahmed *et al.* explored the use of gadolinium-doped ceria (GDC) to optimize the anode microstructure of intermediate-temperature SOFCs (IT-SOFCs) and increased the peak power density to 48.62 mW cm^{-2}.[30] Li *et al.* focused on optimizing the composition of samarium strontium manganite-yttria stabilized zirconia (SSM-YSZ) cathodes to enhance their electrochemical performance in IT-SOFCs.[31] The optimal loading amount was 18 wt% $Sm_{0.5}Sr_{0.5}MnO_3$ (SSM55), and the planned resistance of the prepared electrode could be reduced to 0.17 Ω cm^2. Kuterbekov *et al.* significantly improved the efficiency, durability, and environmental sustainability of SOFC technology by combining a ceria-doped electrolyte and a composite anode.[32] The study found that the composite anode with graded porosity achieved a power density of 1.2 W cm^{-2} and remained stable for 5000 hours with a degradation rate of less than 1% per 1000 hours.

However, traditional SOFC structure optimization methods—experimental trial-and-error, simulations, and conventional techniques (mathematical, heuristic, simple hybrids)—face low efficiency, high costs, and difficulty finding global optima.[27] These methods face several limitations, including low efficiency, high costs, and challenges in identifying the global optimal solution.[33] Traditional mathematical methods such as gradient descent and linear programming rely on explicit mathematical models or physical mechanisms for their accuracy. They struggle to handle complex structures with high dimensionality and strong nonlinearity.[34] Single heuristic methods, such as particle swarm optimization (PSO), corely rely on heuristic rules to efficiently search the solution space. During the optimization process, they need to frequently call physical models to evaluate the quality of solutions, which is not only inefficient but may also lead to insufficient accuracy of the final optimization scheme due to the accumulation of evaluation errors.[35] Even simple hybrid methods that combine mathematical models with basic heuristics often fail to fully capture the intricate parameter interactions in SOFCs, resulting in suboptimal outcomes.[36] Experimental trial-and-error approaches demand significant time and resources,[37,38] while numerical simulation methods, although capable of providing deeper insights into underlying mechanisms, incur high computational costs and are impractical for large-scale parameter optimization.[39] Furthermore, the complex interactions among SOFC structural parameters are often difficult to fully account for using these traditional approaches, resulting in suboptimal optimization outcomes that fall short of expectations.

To overcome these challenges, machine learning (ML), as a data-driven method, enables SOFC performance prediction and optimization. ML can automatically learn complex nonlinear relationships from large experimental or simulation data to establish efficient predictive models.[40–42] Xu *et al.* combined computational fluid dynamics (CFD) with an artificial neural network (ANN) to optimize SOFC power output to 0.63 W cm^{-2} *via* operational adjustments.[43] However, their study emphasized comparative analysis with the baseline CFD model, lacking experimental validation for methodology effectiveness. In addition, the "white-box" SHAP (SHapley Additive exPlanations) method enhances the interpretability of "black-box" ML models.[44] SHAP quantifies each input feature's contribution to predictions, providing intuitive feature importance analysis. Kim *et al.* used ML to predict proton ceramic fuel cells (PCFCs) and identify key factors affecting cell performance through feature importance analysis, providing data-driven insights for PCFCs.[45] However, their limited dataset (591 points) and operational confounding effects led to an R^2 of 0.85, with poor generalization; lacking experimental verification weakened conclusions' credibility and practical value.

This study proposes a new ML-based AS-SOFC design approach, including four modules: thermal-electro-chemical-mechanical multiphysical modeling and evaluation, database construction based on multiphysical simulations, predictive model building in ML algorithms, parameter optimization and experimental verification, to guide the rational design of SOFC button cell structure. First, the microscopic parameters of a single button cell sample are obtained by 3D reconstruction. Then, the multiphysical model is established and verified using the measured data of the sample. Then, the maximum power (P_{max}) and failure probability (P_f) databases are constructed through TECM simulations by varying the thickness and microscopic parameters (22 features) of the cell. Next, feature engineering is used to identify the 10 key features that affect P_{max} and P_f, and predictive models for these two target quantities are established respectively. Finally, random forest (RF) and genetic algorithm (GA) are used to for structural optimization.[46,47] The optimal combination of key features is determined under the constraints of failure probability below 0.632 and maximum power density. Based on the optimization results, the cathode is designed and the optimized cell is measured to verify the reliability and feasibility of the proposed method. Additionally, the interpretable SHAP method is introduced to

analyze the importance of and interactions between macro- and microscopic parameters, and how they influence the performance and failure probability of the cell to be designed.

2. Experimental

2.1 Preparation of AS-SOFC

The AS-SOFC button cells in this work were prepared based on commercial half-cells (Ningbo SOFCMAN Energy Technology Co., Ltd, China), comprising a NiO/3YSZ anode support, a NiO/8YSZ anode functional layer (AFL), an 8YSZ electrolyte, and a gadolinium-doped ceria (GDC) buffer layer. The cathode of the cell was prepared by screen printing. The screen-printing ink with a solid content of 65 wt% was prepared using commercial $La_{0.6}Sr_{0.4}Co_{0.2}Fe_{0.8}O_{3-\delta}$ powder (LSCF, Fuel Cell Materials, USA). A 3 : 1 mixture of pine alcohol and turpentine was used as a solvent and first mixed with 2.2 wt% polyvinyl butyral (PVB, Shanghai Macklin Biochemical Co., Ltd, China) powder. Then LSCF powder, 1.3 wt% dispersant triethanolamine (TEA, Shanghai Aladdin Biochemical Technology Co., Ltd, China) and 3 wt% plasticizer dioctyl phthalate (DOP, Shanghai Aladdin Biochemical Technology Co., Ltd, China) were added in sequence. The mixture was uniformly mixed with a self-rotating and revolving vacuum mixer (MV300SVII, Simai Co., Ltd, Japan) for 5 min and finally ground with a three-roller grinder (ZYTR-50, Guangdong ZhongYi Technology Co., Ltd, China) to obtain the LSCF ink. LSCF ink was screen-printed onto half-cells (D = 1.5 cm, t = 414 μm) for the cathode layer. An initial reference sample was prepared by screen-printing LSCF ink on the as-received half-cell, followed by debinding at 500 °C for 1 h and sintering at 800 °C for 2 h.

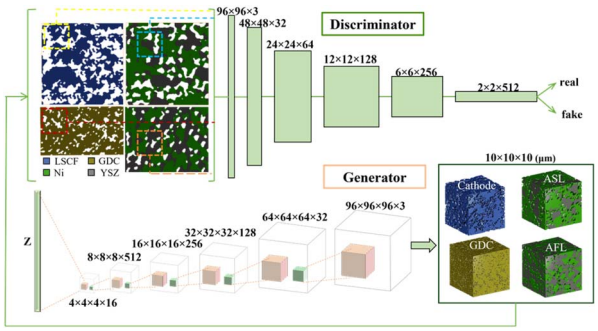

Fig. 1 GAN network structure for generating 3D microstructures from 2D slices.

2.2 3D reconstruction and electrochemical analysis

The microstructure of each layer of the full cell was analyzed using a cross-section polisher (CP, JEOL, Japan) and a scanning electron microscope (SEM, Hitachi, Japan), as shown in Fig. S1(a). A focused ion beam scanning electron microscope (FIB-SEM, Carl Zeiss Crossbeam 350) was used to prepare a cross-section of the button cell with the ion beam and to image the 2D microstructures of the cross-section using the InLens detector, as shown in Fig. S1(b)–(f). SliceGAN[48] was used to obtain the 3D microstructure of the cell based on FIB slices, and its network architecture is shown in Fig. 1. Based on the Avizo 3D platform, the microscopic parameters of each part of SOFC were calculated and the results are shown in Table 1. The i–V curves were measured using an electrochemical workstation (Interface 5000e, Gamry, USA) at an operating temperature of 800 °C. Pt paste was screen-printed onto the surfaces of the two electrodes of the cell as the current collector. The button cell was placed on an alumina tube and sealed with ceramic sealant (552-VFG, AREMCO, USA). The anode side was fed with 100 sccm of hydrogen, and the cathode side was exposed to air. The specific measurement setup is shown in Fig. S2, and the operating environment parameters are summarized in Table 1.

3. Multiphysics coupled model

A multiphysics model including electrochemical reaction, gas flow, species diffusion, heat transfer and thermal stress was established, and the failure probability (P_f) caused by these processes was calculated. According to the actual test device, this study adopted 2D axisymmetric geometry modeling, as shown in Fig. 2(a). The main governing equations of each physical process are shown in Table 2. By fitting the test results of the initial reference sample, the invariant reference current densities $i^{a}_{0,TPB}$ and $i^{c}_{0,DPB}$ were obtained, corresponding to the anode and cathode, which were 0.0026 A m^{-1} and 7.8 A m^{-2} respectively. The comparison between the fitted simulation model and the measurement results is shown in Fig. 2(b).

It should be noted that in order to improve the controllability of optimizing microscopic parameters in the experimental system, this model uses Bruggeman relation[54] and percolation theory[55,56] to describe the relationship between microscopic parameters and microscopic morphology. The tortuosity of each section, the three-phase boundary (TPB) density on the anode side, and the two-phase boundary (DPB) density on the cathode side can be calculated by the following formula:

$$\tau = \varepsilon^{-1/2} \quad (1)$$

Table 1 Geometric, microscopic and operating parameters of initial SOFC samples

Parameters	Value
$x^0_{H_2}, x^0_{H_2O}, x^0_{O_2}, x^0_{N_2}, T^0, V_{oc}$	0.97, 0.03, 0.21, 0.79, 1073.2 K, 0.7 V
t^{as}, t^a, t^e, t^{gdc}, t^c, D^a, D^c (mm)	0.39, 0.0074, 0.0127, 0.00436, 0.01685, 15, 10
ε^{as}, ε^a, ε^c, ϕ^{as}_{Ni}, ϕ^{as}_{YSZ}, ϕ^{a}_{Ni}, ϕ^{a}_{YSZ}, ϕ^{c}_{LSCF}, θ^a, θ^c, P^a, P^c, P^c_e(1)	0.202, 0.15, 0.404, 0.424, 0.374, 0.35, 0.5, 0.596, 0.4346, 0.6857, 0.807, 0.998, 1
d^{as}_p,d^{as}_{Ni},d^{as}_{YSZ},d^{a}_p,d^{a}_{Ni},d^{a}_{YSZ}, d^{c}_p,d_{LSCF} (nm)	703.44, 373.15, 563.8, 398.06, 242.82, 1337.87, 901.04, 450.91

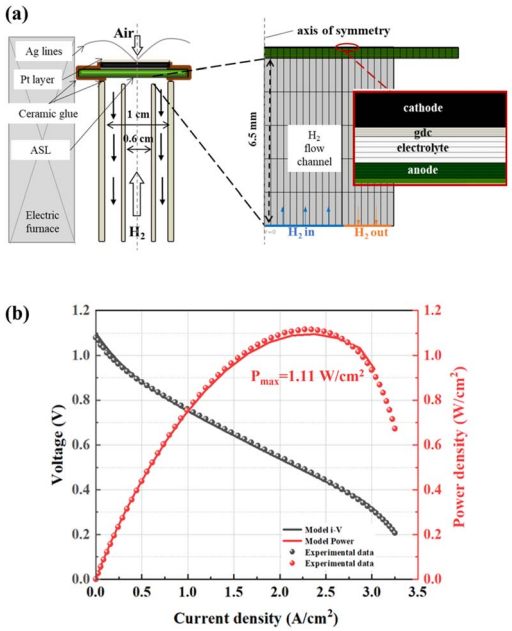

Fig. 2 Establishment of the multi-physics coupling model: (a) schematic diagram of the button cell test (left) and schematic diagram of the 2D axisymmetric geometric model and mesh configuration (right); (b) *i–V* curve and power density curve of the simulation and test results.

$$l^{a}_{TPB} = 6 \times \frac{\min\left(d^{a}_{YSZ}, d^{a}_{Ni}\right)}{\left(d^{a}_{Ni}\right)^{3}} \cdot (1-\varepsilon^{a}) \cdot \sin\theta^{a} \cdot \phi^{a}_{Ni} \cdot \chi^{a}_{e} \cdot \chi^{a}_{ion} \cdot Z_{Ni,YSZ} \quad (2)$$

$$S^{c}_{DPB} = \pi d^{2}_{LSCF} n^{V}_{LSCF} \chi^{c}_{e} \chi^{c}_{ion} + \gamma_{LSCF,e} n^{S}_{LSCF} \chi^{c}_{e} \quad (3)$$

where τ is the tortuosity, ε is the porosity, ϕ is the volume fraction, d is the average particle size, and θ is the contact angle. The superscripts a and c represent the anode and cathode, respectively, the subscripts e and ion represent the electronic phase and the ionic phase, respectively, and the superscripts S and V represent the contact surface between the electrolyte and the electrode and the electrode body, respectively. n^{V}_{LSCF} and n^{S}_{LSCF} represent the number of LSCF particles per unit volume and per unit electrolyte surface area, respectively, and $\gamma_{LSCF,e}$ represents the electrochemical reaction site at each contact between the LSCF particles and the dense electrolyte. The calculation formulas are as follows:[55,57]

$$n^{V}_{LSCF} = \frac{6 \cdot (1-\varepsilon^{c}) \cdot \phi_{LSCF}}{\pi \cdot d^{3}_{LSCF}} \quad (4)$$

$$n^{S}_{LSCF} = \frac{6 \cdot (1-\varepsilon^{c}) \cdot \phi_{LSCF}}{\pi \cdot d^{2}_{LSCF}} \quad (5)$$

$$\gamma_{LSCF,e} = \pi \cdot d_{LSCF} \cdot \sin\theta^{c} \quad (6)$$

Among them, χ represents the percolation probability, which is used to describe the probability of forming a permeable path in the composite medium. For the Ni-YSZ anode, the active length of TPB depends on the probability of simultaneous percolation of Ni/YSZ/H_2; for the LSCF cathode, the active DPB depends on the probability of simultaneous percolation of LSCF/O_2. In this paper, the proportion χ of the penetrating reaction interface is obtained through the 3D microstructure, as shown in Fig. S3. So, for the anode χ^{a} and the cathode χ^{c}:

$$\chi^{a} = \chi^{a}_{e} \cdot \chi^{a}_{ion} \cdot Z_{Ni,YSZ} \quad (7)$$

$$\chi^{c} = \chi^{c}_{e} \cdot \chi^{c}_{ion} \quad (8)$$

4. Predictive model

The power density and failure probability of SOFC are affected by the synergistic effects of its macroscopic and microstructural parameters. Therefore, the macro- and microstructural parameters of the SOFC simulation model were swept while keeping

Table 2 Governing equations of multiphysics coupled model

Physical process	Equations	Theoretical model
Electrochemical reaction	$i^{a} = l^{a}_{TPB} i^{a}_{0,TPB} \left[\frac{p^{H_2}}{p^{H_2}_{ref}} \exp\left(\frac{2F(\eta^{a}_{act}+\eta^{a}_{conc})}{RT}\right) - \frac{p^{H_2O}}{p^{H_2O}_{ref}} \exp\left(\frac{F(\eta^{a}_{act}+\eta^{a}_{conc})}{RT}\right) \right]$	Butler–Volmer equation[49]
	$i^{c} = S^{c}_{DPB} i^{c}_{0,DPB} \left[\exp\left(\frac{1.2F(\eta^{c}_{act}+\eta^{c}_{conc})}{RT}\right) - \frac{p^{O_2}}{p^{O_2}_{ref}} \exp\left(\frac{F(\eta^{c}_{act}+\eta^{c}_{conc})}{RT}\right) \right]$	
Gas flow	$\nabla \cdot (\rho \boldsymbol{v}) = S_{mass}$	Navier–Stokes equation[50]
	$\rho \boldsymbol{v} \cdot \nabla \boldsymbol{v} = -\mathbf{I}\nabla p + \nabla \cdot \left[\mu(\nabla \boldsymbol{v} + \boldsymbol{v}\nabla) - \frac{2}{3}\mu \mathbf{I} \nabla \boldsymbol{v} \right] - \boldsymbol{v}\dot{S}_{mass}$	
Species diffusion	$\boldsymbol{j}_i = -\rho D^{mK}_{i} \nabla \omega_i - \rho \omega_i D^{mK}_{i} \frac{\nabla M}{M} + \rho \omega_i \sum_k \frac{M_i}{M} D^{mK}_{i} \nabla x_i$	Stefan–Maxwell equation[38]
Heat transfer	$\nabla \cdot (-\lambda_{eff} \nabla T) + \rho C_p \boldsymbol{v} \cdot \nabla T = Q_{ohm} + Q_{act} + Q_{entr}$	Energy Conservation[51]
Stress–strain	$\boldsymbol{\varepsilon} = (\nabla \mathbf{u} + \mathbf{u}\nabla)/2;\ \nabla \cdot \boldsymbol{\sigma} + \boldsymbol{f} = 0;\ \boldsymbol{\sigma} = \boldsymbol{C} : \boldsymbol{\varepsilon}$	Continuum Mechanics[52]
Failure probability	$P_f = 1 - \prod_{i=1}^{i=3} \exp\left[-\int_V \left(\frac{\sigma_i}{\sigma_W}\right)^{m} \frac{dV}{V_0} \right]$	Weibull method[53]

the operating conditions unchanged, including 22 features such as layer thickness, porosity, component content, and particle size. The dataset included two target variables: maximum power density (P_{max}) and failure probability (P_f), with a size of 2000 groups.

Then an accurate predictive model is established here. It mainly includes three steps: (a) evaluate 15 common ML algorithms to select the most suitable model, (b) find key features through feature engineering, (c) establish a predictive model and evaluate it. The regression coefficient of determination (R^2) and root mean square error (RMSE) were used to evaluate these models. The mathematical expressions are shown in eqn (9) and (10) respectively.[58,59]

$$R^2 = 1 - \frac{\sum_{i=1}^{n} (y_i - y_i^*)^2}{\sum_{i=1}^{n} (y_i - \bar{y})^2} \quad (9)$$

$$\mathrm{RMSE} = \sqrt{\frac{1}{n} \sum_{i=1}^{n} (y_i - y_i^*)^2} \quad (10)$$

where y_i is the actual value, y_i^* is the predicted value of the ML model, and $\bar{y}$ is the mean of the actual values.

4.1 Predictive model algorithm screening

In this work, in order to screen out the algorithm suitable for performance predictions of SOFCs, 15 widely used ML algorithms were introduced to construct P_{max} and P_f predictive models based on SOFC macro-microstructure parameters, including linear regression (LR), decision tree regression (DT), random forest regression (RF), K nearest neighbor regression (KNN) and support vector machine (SVM), *etc.* For this purpose, the dataset was randomly divided into two subsets, namely training set and test set, with a ratio of 2 : 1, for the task of model training and testing.

Fig. 3 summarizes the RMSE and R^2 of all 15 ML algorithms for predicting (a) P_{max} and (b) P_f. R^2 is between 0 and 1, and the closer its value is to 1, the more accurate the predictive model is. RMSE can be directly interpreted as the average difference between the predicted value and the true value, and the smaller its value is, the more accurate the predictive model is. It can be seen that the RMSE of the RF for the test set prediction of P_{max} and P_f are the smallest and the R^2 are greater than 0.9. According to the above analysis, RF shows the best regression performance for the predictive models of P_{max} and P_f when RMSE is minimum and R^2 is maximum. Therefore, RF is used to predict the electrical performance and failure probability of SOFC in this study.

4.2 Feature selection

To improve the performance of the RF predictive model, we performed a three-step feature selection to obtain the key features for predicting P_{max} and P_f. It is worth noting that we select the same key features for the two target variables P_{max} and P_f, aiming to ensure that the impact of the features on the two target variables is taken into account during the GA optimization process. The first step is to remove features with high correlation. Fig. 4(a) and (b) show the Pearson correlation coefficients between the top 15 features of the P_{max} and P_f predictive models, respectively. Except for the expected strong correlation ($r = -1$) between the cathode layer porosity (poro_c) and the LSCF volume fraction (LSCF_c), Pearson correlation analysis showed that there was no significant correlation between other structural features ($|r| < 0.8$), which confirmed the independent influence mechanism of each feature on the target performance index.

The second step is to use the RF algorithm to rank the features by importance. Here, the importance of the features to the target quantities P_{max} and P_f are taken into account at the same time. Therefore, the features are sorted according to the sum of the importance coefficients of the two target quantities, as shown in Fig. 4(c). Features that contribute little to the predictive model (importance coefficient <0.002) are deleted, and features ranked by importance are stored as candidate feature sequences.

The third step is to extract key features. Starting from the empty set, features are gradually added to the target feature subset from the candidate feature sequence. RF regression is used for prediction to obtain the R^2 curves of the P_{max} and P_f predictive models with the number of features, as shown in

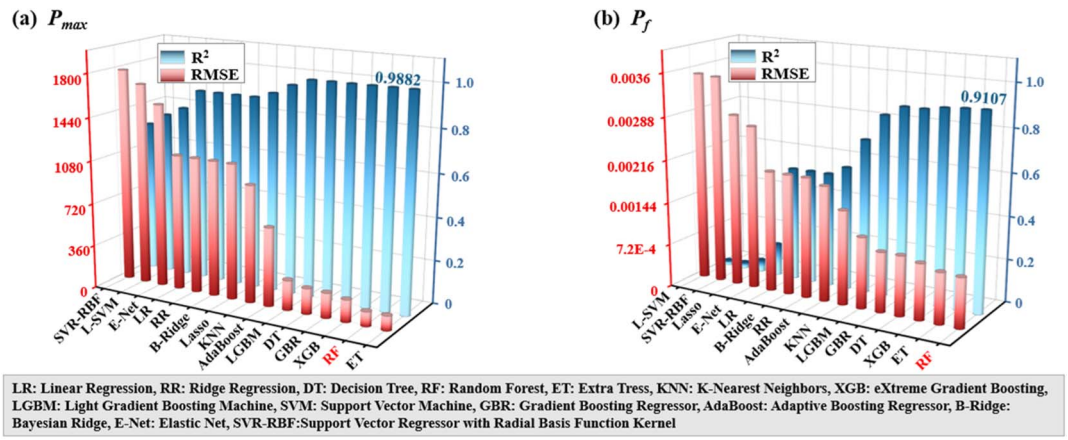

Fig. 3 R^2 and RMSE of each algorithm for (a) P_{max} and (b) P_f predictive models.

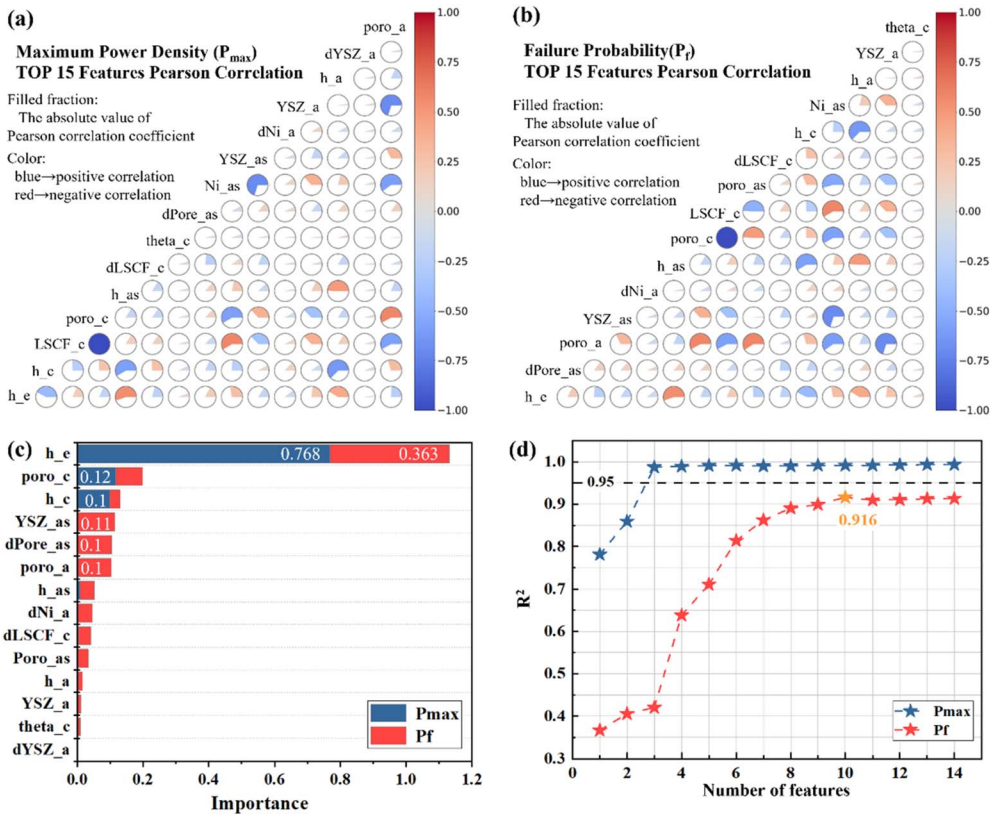

Fig. 4 The process of feature selection. (a) and (b) Removing highly correlated features. (c) Ranking features by the sum of their importance, P_{max} and P_f. (d) Selection of key features.

Table 3 Key features of P_{max} and P_f predictive models

Abbreviation	Description
h_e	The thickness of the electrolyte layer (EL)
poro_c	Porosity of cathode layer
h_c	The thickness of cathode layer
YSZ_as	Volume fraction of YSZ in the anode support layer (ASL)
dPore_as	The average diameter of the ASL pores
poro_a	Porosity of anode
h_as	Thickness of ASL
dNi_a	The average diameter of Ni particles in the anode layer
dLSCF_c	The average diameter of LSCF particles in the cathode layer
poro_as	Porosity of ASL

Fig. 4(d). It can be seen that when the first 3 features are input, the R^2 of the predictive model of P_{max} is greater than 0.95, and remains stable as the number of features increases. The R^2 of the predictive model of P_f reaches the maximum when the first 10 features are input. Therefore, the first 10 features are selected as the key features of the P_{max} and P_f predictive models, as shown in Table 3.

4.3 Predictive model construction

RF integrates the prediction results of multiple decision trees and is a ML method that uses voting or averaging mechanisms to improve accuracy and robustness.[60] For regression problems, the prediction formula of RF is the average value of the output of each decision tree, which is mathematically expressed as:[61]

$$y^* = \frac{1}{N}\sum_{i=1}^{N} y_i^*(x) \quad (11)$$

Here, grid search (GridSearchCV)[62] is used to optimize the hyperparameters of the RF model, and different parameter search spaces are customized for the two targets. The optimal parameter combination is determined through 5-fold cross-validation, as shown in Table 4. 70% of the dataset is used as the training set, and the rest 30% is used as the test set. Training is performed according to the optimized parameters, and the topology diagram is shown in Fig. 5.

Table 4 Hyperparameter optimization of RF predictive model for P_{max} and P_f

Hyperparameters	P_{max}	P_f
bootstrap	True	True
max_depth	None	None
max_features	0.9	0.9
min_samples_leaf	1	1
min_samples_split	2	2
n_estimators	100	500
random_state	42	42
n_jobs	4	4

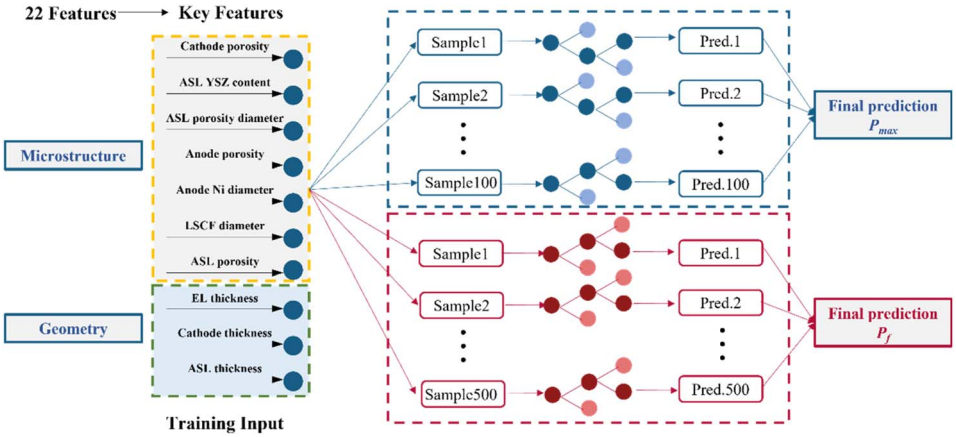

Fig. 5 Topological diagram of the RF predictive models for P_{max} and P_f.

5. Results and discussion

5.1 Predictive model evaluation

R^2 and RMSE were used as indicators to evaluate the P_{max} predictive model and P_f predictive model, and the results are shown in Fig. 6(a) and (c). As shown in the figures, the closer the colored solid line is to the diagonal line, the closer the predicted value is to the actual value. The R^2 of the P_{max} predictive model in both the training set and the test set is greater than 0.99, showing excellent prediction ability. The prediction performance of the P_f predictive model in the training set and the test set is slightly worse. However, its R^2 is not less than 0.95, which also shows good prediction ability.

Here, we also introduced 10-fold cross-validation (10-Fold CV) and leave-one-out cross validation (LOOCV) to more reliably

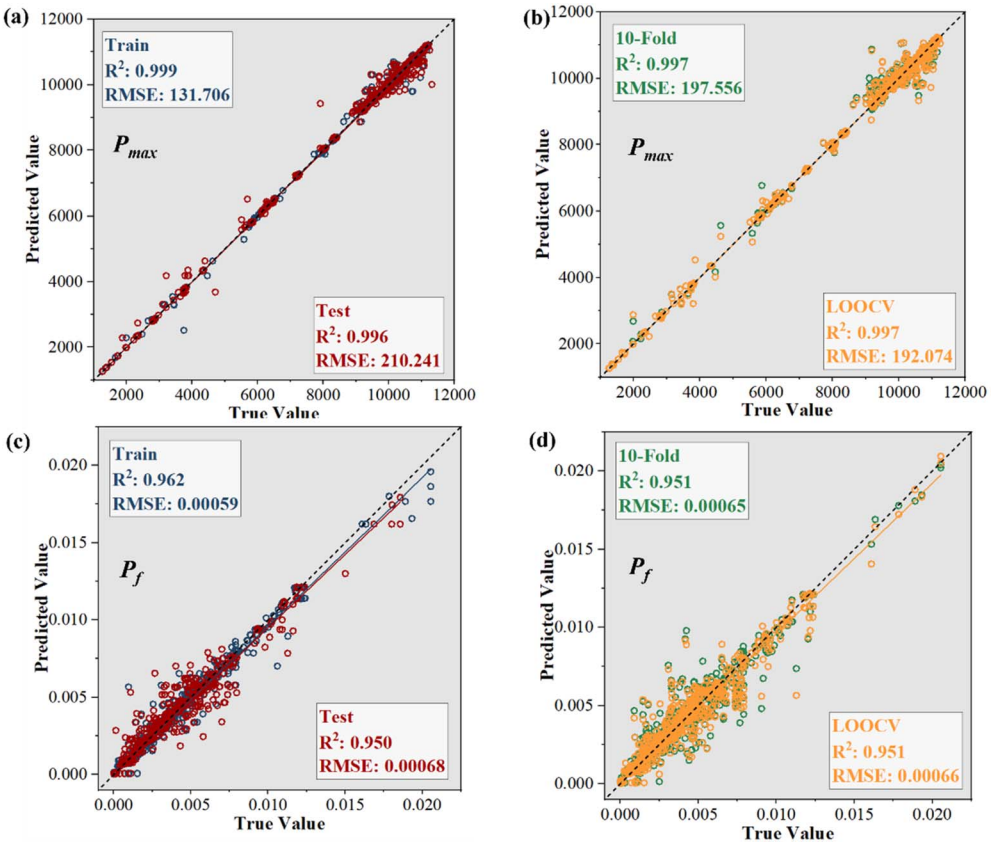

Fig. 6 Evaluation of the P_{max} predictive model on the test and training sets (a) and 10-fold crossover and LOOCV validation of the training set (b); evaluation of the P_f predictive model on the test and training sets (c) and 10-fold crossover and LOOCV validation of the training set (d).

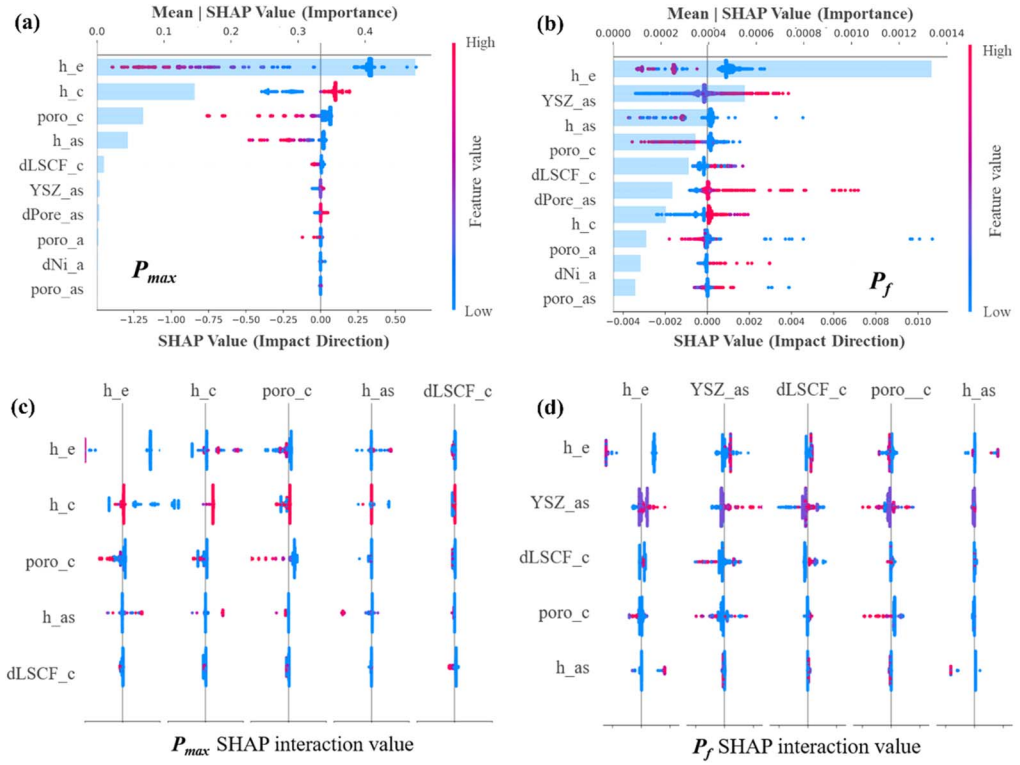

Fig. 7 SHAP analysis of the predictive models. SHAP feature importance combination plot of (a) P_{max} predictive model and (b) P_f predictive model; SHAP feature interaction plot of (c) P_{max} predictive model and (d) P_f predictive model.

estimate the generalization ability of models, as shown in Fig. 6(b) and (d).

Similarly, the closer the scatter distribution trend is to the reference line (slope $k = 1$), the more accurate the predictive model is. The R^2 of P_{max} predictive model and P_f predictive model are both greater than 0.95, and there is no abnormality in RMSE. This shows that both predictive models have excellent generalization ability.

In addition, SHAP analysis was employed to elucidate feature relationships with P_{max} and P_f (Fig. 7). The honeycomb diagram shows the direction of the influence of the features on the prediction results and the importance ranking, and the bar chart shows the average value of the absolute SHAP value. The honeycomb diagram consists of each sample point, and the symbol of the SHAP value represents the direction of influence on the target quantity (enhancement/weakening). The deeper the red color, the greater the value of the feature. On the contrary, the deeper the blue color, the smaller the value of the feature. The bar chart shows the importance of each feature. Notably, Fig. 7(a) demonstrates that electrolyte thickness (h_e) exerts the predominant negative effect on P_{max}, corroborating Park *et al.*'s findings where reducing it to 2.5 μm significantly improved power density.[63] Conversely, Fig. 7(b) shows that failure probability rises with increasing h_e, primarily due to temperature gradient distribution. Thicker electrolytes possess greater structural strength, enabling better thermal gradient absorption and redistribution, thus reducing local stress concentration (Fig. S4). In addition, Fig. 7(b) quantitatively illustrates how YSZ content in the anode support layer critically affects P_f, aligning with Morales and Vafaeenezhad *et al.*'s bending tests on Ni/YSZ ratios' mechanical impact.[64,65] Regarding performance indicators, higher maximum power density (P_{max}) and lower failure probability (P_f) are desirable, corresponding to right-shifted scatter in Fig. 7(a) and left-shifted in Fig. 7(b). Interestingly, most features exert opposite effects on the two targets. For example, cathode thickness (h_c) and ASL pore size (dPore_as) positively impact P_{max}, but increase failure risk; while electrolyte thickness (h_e) and cathode porosity (poro_c) negatively affect P_{max}, yet reduce failure probability. Because increasing cathode thickness expands the reaction interface (DPB), enhancing oxygen reduction reaction (ORR), while larger ASL pore size improves hydrogen transport, reducing concentration polarization and boosting power density. However, at high current density, the heat released by the electrochemical reaction is concentrated, causing local overheating of the cell and inducing thermal stress, as shown in Fig. S5. Therefore, the optimization of SOFC needs to consider these two target quantities (P_{max} and P_f).

Fig. 7(c) and (d) show the interaction diagrams of the top five features, that is, the impact of the joint effect between the features on the prediction results. For power density, there is a relatively obvious interactive relationship between electrolyte thickness (h_e), cathode thickness (h_c) and cathode porosity (poro_c). For example, when h_c and poro_c increase at the same time, the predicted maximum power density shows a significant increase trend, as shown in Fig. 7(c). This is

because the increase in h_c expands the axial active area of the oxygen reduction reaction, and the increase in poro_c enhances the transport of oxygen, as shown in Fig. S6. The synergistic effect of the two makes the number of active sites increase by multiples. Similarly, when the YSZ content (YSZ_as) and electrolyte thickness (h_e) of the ASL increase simultaneously, the failure probability is significantly reduced, as shown in Fig. 7(d). This is because the increase in YSZ_as increases the rigidity modulus of ASL, while the increase in h_e reduces the thermal stress of the electrolyte. Therefore, the combined effect of the two parameters significantly reduces the failure probability caused by thermal expansion mismatch.

Table 5 The scope of key features and optimal solution in GA optimization algorithm

Key features	Unit	Value range	Optimal solution
h_e	μm	(0.5, 300)	1.98
poro_c	1	(0, 1)	0.342
h_c	μm	(1, 50)	39.29
YSZ_as	1	(0, 1)	0.480
dPore_as	nm	(400, 2000)	1658.05
poro_a	1	(0, 1)	0.362
h_as	μm	(40, 4000)	490.43
dNi_a	nm	(50, 600)	198.71
dLSCF_c	nm	(300, 800)	383.04
poro_as	1	(0, 1)	0.282

5.2 Optimization and experimental validation

Based on the obtained predictive models and analysis, we use genetic algorithm (GA)[66] to perform conditionally constrained single-objective optimization. The purpose of this is to find the optimal characteristic combination that maximizes the SOFC power density within a critical failure probability. In addition, through a simple cathode optimization experiment, SOFC button cells were prepared and measured according to the optimal feature combination to verify the feasibility of the entire optimized approach.

Here, based on the RF predictive model of the power density, the GA is adopted to optimize the macro- and microstructural parameters of SOFC. As a global optimization algorithm based on natural selection and genetic mechanisms, GA has significant advantages in the field of structural optimization. The GA used in this paper is implemented based on DEAP (Distributed Evolutionary Algorithm Framework) and adopts the classic evolutionary computing paradigm. We encode each individual as a key feature vector (10 dimensions) and predict the values of P_{max} and P_f by calling the RF predictive model in Section 4.3. The fitness value is calculated according to the constraint on the failure probability ($P_f < 0.632$), and the solution that does not meet the constraint is assigned a negative infinite fitness. The detailed calculation framework is shown in Fig. 8(a). The 0.632 failure probability threshold is adopted because it aligns with the standard definition of characteristic strength in structural reliability analysis, where it represents the

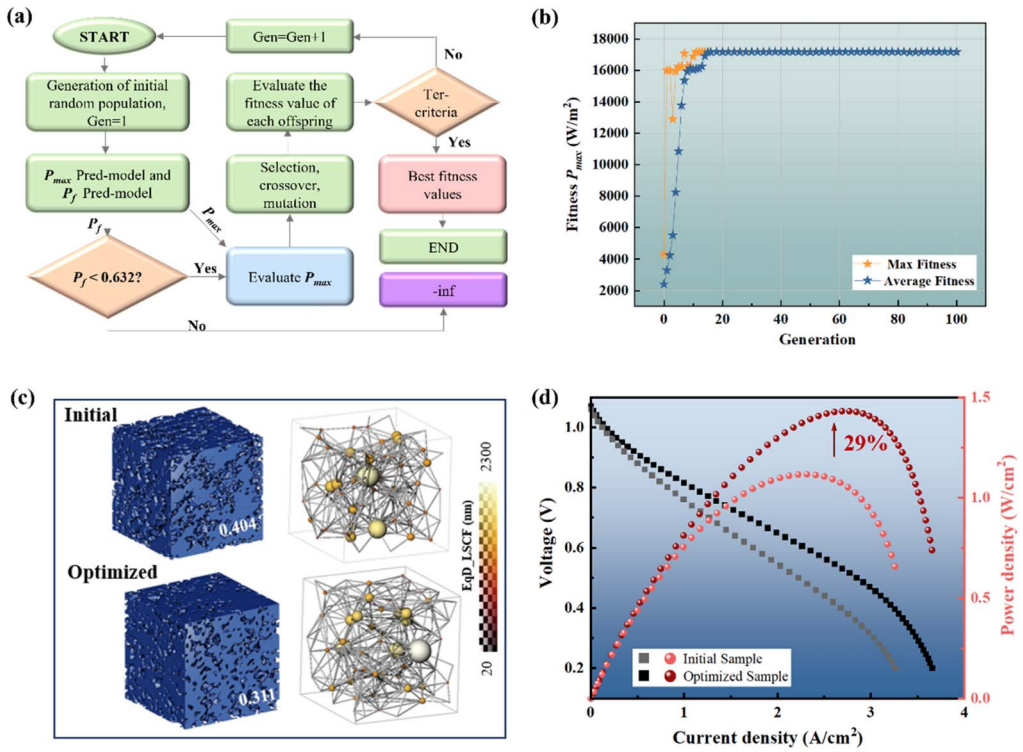

Fig. 8 Optimization and experimental verification results. (a) Flowchart of the collaborative optimization of the RF predictive model and GA; (b) the change of optimized fitness with generation; (c) the 3D microstructure of the cathode of the initial sample and the optimized sample; (d) the comparison of the measurement results of the initial sample and the optimized sample.

Table 6 Processing conditions and measured result parameters for initial and optimized samples

Sample	Screen printing layers	Sintering temperature	h_c (μm)	poro_c	dLSCF_c (nm)
Initial	1	800 °C	16.85	0.404	450.91
Optimized	2	1000 °C	36.60	0.311	627.21

failure probability of a reference structure under uniform uniaxial stress conditions.[67] Through this optimization framework, the optimal features values that can achieve the maximum power density as much as possible without being easily damaged can be found.

In addition, considering the realistic constraints and avoiding the generation of invalid solutions, conditional restrictions were added to each feature, as shown in Table 5. After 100 generations of evolution, the GA optimization algorithm reached convergence, as shown in Fig. 8(b). The figure shows that max fitness and average fitness increase rapidly first, then fluctuate and finally stabilize as the number of evolutionary generations increases. The average fitness curve gradually converges towards the max fitness curve and almost overlaps. This shows that the algorithm successfully achieves a balanced transition from global exploration to local exploitation and converges to a high-performance, consistency solution set under constraints. The optimal characteristic values obtained are shown in Table 5. The optimized P_{max} can reach 1.67 W cm^{-2}.

Among the 10 key features, cathode-related thickness (h_c), porosity (poro_c) and LSCF average particle size (dLSCF_c) have important effects on the electrochemical and mechanical properties of SOFC cells. Therefore, the features values of other parts are fixed and kept as the measured values of the initial sample, as shown in Table 1. The cathode features values (h_c, poro_c and dLSCF_c) are optimized through the above-mentioned RF and GA collaborative optimization approach. The optimal solutions are 36.8 μm, 0.312, and 608 nm, respectively, and the maximum power density is 1.45 W cm^{-2}.

Experimentally, we used the same LSCF ink and prepared the required cathode layer by adjusting the number of screen-printing layers and sintering temperatures. According to the comparison of the cathode structural parameters before and after optimization, its thickness was increased by adding a layer of screen-printed LSCF layer, and its particle size was increased by increasing the sintering temperature from 800 °C to 1000 °C. The processing conditions of the initial sample and the optimized sample are shown in Table 6, and the cross-sectional SEM and FIB slice images are shown in Fig. S1 and S7, respectively.

As with the initial sample, the cathode of the optimized sample was sliced by FIB and reconstructed 3D using sliceGAN. Fig. 8(c) illustrates the 3D microstructures of the cathodes from both the initial sample and the optimized sample. It can be seen that the cathode porosity of the optimized sample is reduced and the average particle size of the LSCF particles is increased. The microstructural parameters were obtained by the Avizo 3D platform, and the comparison with the initial sample is shown in Table 6. After the same working condition measurement, the maximum power density of the optimized sample is 1.43 W cm^{-2}, which is 29% higher than that of the initial sample, as shown in Fig. 8(d).

Please note that all structural parameters of the experimentally prepared LSCF cathode cannot be completely equal to the values given by the cathode optimization. Here, the macroscopic and microstructural parameters we obtained through simple experiments are different from the optimized values. Therefore, the measured results (1.43 W cm^{-2}) are slightly smaller than the optimal values predicted by the optimization approach (1.45 W cm^{-2}). Nevertheless, by trying to get close to the optimal values of the optimization approach, the electrical performance has been improved by nearly 30%. This verifies the effectiveness of the optimization approach in practice. In addition, we have incorporated a comprehensive stress analysis of the optimized cell through our multiphysical modeling approach, as shown in Fig. S8. The analysis reveals that the electrolyte surface exhibits no significant stress concentration, with temperature variations remaining below 5 K. The calculated failure probability of 0.0205 is substantially lower than the conventional threshold value of 0.632, confirming that the optimized cell configuration maintains stable structural reliability under operational conditions. By combining the multi-scale simulation of sintering, it is hoped that the inverse design of sintering process parameters can be achieved in the future, and the design process can be optimized as needed.

6. Conclusion

This study aims at the problems of low experimental iteration efficiency and insufficient parameter space exploration in the macro-microstructure optimization of traditional solid oxide fuel cells (SOFCs). We proposed a collaborative optimization approach for anode-supported SOFCs based on machine learning (ML), and verified its effectiveness through experiments. Our approach synergistically integrates microstructure characterization, multiphysical modeling, and ML to achieve unprecedented macro-micro design capabilities. The key innovations include: (1) data-driven parameterization that replaces literature-based assumptions, significantly improving model accuracy; (2) a hybrid finite element analysis (FEA)-ML framework that enhances dataset robustness while reducing experimental costs; and (3) an RF-GA optimization loop that enables efficient parameter search. The modular architecture further extends the framework's applicability to multi-objective optimization in various energy systems. The main findings of this study can be summarized as follows:

(1) Through thermal–mechanical–chemical–electrical coupled numerical simulations, a database of SOFC maximum power density and failure probability was constructed. Ten key

characteristic parameters were selected by feature engineering, and high-precision prediction was achieved based on the random forest (RF) regression model (R^2 reached 0.99 and 0.95, respectively), providing an efficient and reliable data-driven method for SOFC macro- and micro-structure optimization.

(2) Through the integrating of RF predictive model and genetic algorithm, the optimal combination of key characteristic parameters was obtained, and the power density was maximized while ensuring that the failure probability was less than 0.632, thus solving the contradiction between performance and reliability in traditional optimization. The optimal combination of macro- and microstructural parameters was achieved and accordingly the maximum power density of 1.67 W cm^{-2} could reached, further verifying the optimization potential of this method.

(3) Based on the optimization results, experiments on SOFC button cells prepared by regulating the cathode showed that their maximum power density reached 1.43 W cm^{-2}, an increase of 29% over the initial sample, verifying the feasibility and engineering applicability of the proposed optimization approach.

(4) SHAP analysis reveals the competitive effects of key features on power density and failure probability, emphasizes the necessity of multi-objective optimization, and provides clear parameter regulation directions for SOFC material and structure design.

The proposed ML-assisted optimization framework in this study not only significantly enhances the R&D efficiency of SOFCs but also extends its "simulation-data-experiment" closed-loop strategy to the optimization design of the entire SOFC processing chain. This includes, but is not limited to, key processing parameters such as slurry rheological properties, sintering schedules (heating ramps and dwell times), and intelligent regulation of operating parameters like operating temperature, fuel composition, and current density. By integrating the sintering simulation method, the microstructure evolution during the cell preparation process can be accurately predicted and controlled, enabling a full-chain closed-loop design from material selection and process optimization to performance prediction. This ultimately achieves precise regulation and optimization of the cell's comprehensive performance.

Author contributions

Li Duan writing – original draft, writing – review & editing, methodology, visualization, formal analysis. Zilin Yan writing – review & editing, supervision, project administration, funding acquisition. Zehua Pan writing – review & editing, resources, funding acquisition. Zheng Zhong writing – review & editing, resources, supervision, funding acquisition.

Conflicts of interest

The authors declare that they have no conflict of interest.

Data availability

The datasets used in this study are publicly available at **https://github.com/zilinyan/Dataset4JMCApaper**, with additional supporting data included in the SI.

Experimental details, characterization data, and additional figures are provided in the SI. See DOI: **https://doi.org/10.1039/d5ta03421c**.

Acknowledgements

This work was supported by the National Natural Science Foundation of China (Grant No. 12172104), the Talent Recruitment Project of Guangdong (2021QN02L892), Shenzhen Science and Technology Program (GXWD20231130153335002, JCYJ20240813105130041 and JCYJ20241202123505008), Guangdong Basic and Applied Basic Research Foundation (2023A1515010723), the Shccig-Qinling Program (SMY-JY202300140C), and the program of Innovation Team in Universities and Colleges in Guangdong (2021KCXTD006).

References

1 K. Kendall and M. Kendall, *High-Temperature Solid Oxide Fuel Cells for the 21st Century: Fundamentals, Design and Applications*, Elsevier, 2015.
2 Z. Luo, Z. Wang, T. Zhu, Y. Song, Z. Lin, S. P. Jiang, Z. Zhu and Z. Shao, *Energy Environ. Sci.*, 2024, **17**, 6873–6896.
3 Y. Lyu, J. Xie, D. Wang and J. Wang, *J. Mater. Sci.*, 2020, **55**, 7184–7207.
4 B. van Veldhuizen, L. van Biert, P. V. Aravind and K. Visser, *Int. J. Energy Res.*, 2023, **2023**, 5163448.
5 J. F. Shin, W. Xu, M. Zanella, K. Dawson, S. N. Savvin, J. B. Claridge and M. J. Rosseinsky, *Nat. Energy*, 2017, **2**, 1–7.
6 X. Wang, L. Shao, S. Hu, Z. Li, H. Guo, J. Zhang, Y. Zhao, X. Lin, B. Nie, Z. Hu and J. Zou, *Energy Environ. Sci.*, 2024, **17**, 8429–8456.
7 S. P. Jiang and Q. Li, in *Introduction to Fuel Cells: Electrochemistry and Materials*, ed. S. P. Jiang and Q. Li, Springer, Singapore, 2022, pp. 357–424.
8 K. A. Kuterbekov, A. V. Nikonov, K. Z. Bekmyrza, N. B. Pavzderin, A. M. Kabyshev, M. M. Kubenova, G. D. Kabdrakhimova and N. Aidarbekov, *Nanomaterials*, 2022, **12**, 1059.
9 D. Sikstrom and V. Thangadurai, *Ionics*, 2024, DOI: **10.1007/s11581-024-05824-7**.
10 H. Yakabe, M. Hishinuma, M. Uratani, Y. Matsuzaki and I. Yasuda, *J. Power Sources*, 2000, **86**, 423–431.
11 C. Mendonça, A. Ferreira and D. M. F. Santos, *Fuels*, 2021, **2**, 393–419.
12 Y. Su, Z. Zhong and Z. Jiao, *Energy Environ. Sci.*, 2022, **15**, 2410–2424.
13 F. Ramadhani, M. A. Hussain, H. Mokhlis and S. Hajimolana, *Renewable Sustainable Energy Rev.*, 2017, **76**, 460–484.
14 J. Peng, D. Zhao, Y. Xu, X. Wu and X. Li, *Energies*, 2023, **16**, 788.

15 H. Tu and U. Stimming, *J. Power Sources*, 2004, **127**, 284–293.
16 J. T. S. Irvine, D. Neagu, M. C. Verbraeken, C. Chatzichristodoulou, C. Graves and M. B. Mogensen, *Nat. Energy*, 2016, **1**, 1–13.
17 B. Zhu, Y. Mi, C. Xia, B. Wang, J.-S. Kim, P. Lund and T. Li, *Energy Mater.*, 2021, **1**, 100002.
18 S. Chen, H. Zhang, F. Wang, H. Miao, J. Zhao, C. Zhang and J. Yuan, *Int. J. Hydrogen Energy*, 2021, **46**, 22062–22078.
19 B. An, J. Yang, Q. Zhang, K. Wang, D. Song and Y. Wang, *Int. J. Hydrogen Energy*, 2024, **80**, 1093–1102.
20 A. A. Bouaiss, M. S. Mimoune, D. Chabane, N. Lebaal, O. Bouaiss and L. Alloui, *J. Solid State Electrochem.*, 2025, **29**, 1907–1927.
21 Z. Niu, V. J. Pinfield, B. Wu, H. Wang, K. Jiao, D. Y. C. Leung and J. Xuan, *Energy Environ. Sci.*, 2021, **14**, 2549–2576.
22 M. Kleitz and F. Petitbon, *Solid State Ionics*, 1996, **92**, 65–74.
23 P. Costamagna, P. Costa and E. Arato, *Electrochim. Acta*, 1998, **43**, 967–972.
24 D. Bhattacharyya, R. Rengaswamy and C. Finnerty, *Chem. Eng. Sci.*, 2007, **62**, 4250–4267.
25 H. Feng, L. Chen, Z. Xie and F. Sun, *J. Power Sources*, 2015, **286**, 406–413.
26 T. Abdullah and L. Liu, *Int. J. Hydrogen Energy*, 2016, **41**, 13632–13643.
27 J. F. Gonçalves, L. F. N. Sá, T. Lopes, J. R. Meneghini and E. C. N. Silva, *Struct. Multidiscip. Optim.*, 2024, **67**, 216.
28 V. A. C. Haanappel, J. Mertens, D. Rutenbeck, C. Tropartz, W. Herzhof, D. Sebold and F. Tietz, *J. Power Sources*, 2005, **141**, 216–226.
29 F. Dong, D. Chen, R. Ran, H. Park, C. Kwak and Z. Shao, *Int. J. Hydrogen Energy*, 2012, **37**, 4377–4387.
30 A. J. Ahmed and P. Sathish, in *2014 3rd International Conference on the Developments in Renewable Energy Technology (ICDRET)*, IEEE, Dhaka, Bangladesh, 2014, pp. 1–4.
31 W. Li, C. Xiong, Q. Zhang, L. Jia, B. Chi, J. Pu and L. Jian, *Electrochim. Acta*, 2016, **190**, 531–537.
32 K. A. Kuterbekov, A. M. Kabyshev, K. Z. Bekmyrza, M. M. Kubenova, G. Kabdrakhimova, I. Abdullayeva and A. T. Ayalew, *Int. J. Low-Carbon Technol.*, 2025, **20**, 353–367.
33 S.-J. Cheng and J.-K. Lin, *Processes*, 2020, **8**, 828.
34 M. Wu, S. Li, H. Chen, W. Duan and M. Shafiee, *J. Electr. Eng. Technol.*, 2022, **17**, 73–84.
35 R. Shirkhani, H. Jazayeri-Rad and S. J. Hashemi, *J. Nat. Gas Sci. Eng.*, 2014, **21**, 1171–1183.
36 C. Blum, J. Puchinger, G. R. Raidl and A. Roli, *Appl. Soft Comput.*, 2011, **11**, 4135–4151.
37 T. Yang, H. Sezer, I. B. Celik, H. O. Finklea and K. Gerdes, *ECS Trans.*, 2015, **68**, 2397.
38 C. Jiang, Y. Gu, W. Guan, J. Zheng, M. Ni and Z. Zhong, *Int. J. Hydrogen Energy*, 2020, **45**, 904–915.
39 X. Zhong, B. Gallagher, S. Liu, B. Kailkhura, A. Hiszpanski and T. Y.-J. Han, *npj Comput. Mater.*, 2022, **8**, 1–19.
40 C. Yang, C. Ren, Y. Jia, G. Wang, M. Li and W. Lu, *Acta Mater.*, 2022, **222**, 117431.
41 S. Zhai, H. Xie, P. Cui, D. Guan, J. Wang, S. Zhao, B. Chen, Y. Song, Z. Shao and M. Ni, *Nat. Energy*, 2022, **7**, 866–875.
42 H. Xin, *Nat. Energy*, 2022, **7**, 790–791.
43 G. Xu, Z. Yu, L. Xia, C. Wang and S. Ji, *Energy Convers. Manage.*, 2022, **268**, 116026.
44 S. M. Lundberg and S.-I. Lee, in *Advances in Neural Information Processing Systems*, Curran Associates, Inc., 2017, vol. 30.
45 J. Kim, J. Baek and M. Choi, *Array*, 2025, **26**, 100407.
46 J. H. Holland, *Adaptation in Natural and Artificial Systems: An Introductory Analysis with Applications to Biology, Control, and Artificial Intelligence*, MIT Press, 1992.
47 Y. Qin, G. Zhao, Q. Hua, L. Sun and S. Nag, *Sustainability*, 2019, **11**, 3290.
48 S. Kench and S. J. Cooper, *Nat. Mach. Intell.*, 2021, **3**, 299–305.
49 Y. Mehdizadeh Chellehbari, K. Adavi, J. Sayyad Amin and S. Zendehboudi, *Energy Convers. Manage.*, 2021, **244**, 114280.
50 M. Andersson, J. Yuan and B. Sundén, *J. Power Sources*, 2013, **232**, 42–54.
51 Z. Zhang, D. Yue, C. He, S. Ye, W. Wang and J. Yuan, *Heat Mass Transfer*, 2014, **50**, 1575–1586.
52 A. Hagen, A. C. Wulff, P. Zielke, X. Sun, B. Talic, I. Ritucci, H. L. Frandsen, S. H. Jensen, W. R. Kiebach and P. V. Hendriksen, *Int. J. Hydrogen Energy*, 2020, **45**, 29201–29211.
53 R. Clague, A. J. Marquis and N. P. Brandon, *J. Power Sources*, 2013, **221**, 290–299.
54 D. A. G. Bruggeman, *Ann. Phys.*, 1935, **416**, 636–664.
55 D. Chen, Z. Lin, H. Zhu and R. J. Kee, *J. Power Sources*, 2009, **191**, 240–252.
56 D. H. Jeon, J. H. Nam and C.-J. Kim, *J. Electrochem. Soc.*, 2006, **153**, A406.
57 P. Costamagna, P. Costa and V. Antonucci, *Electrochim. Acta*, 1998, **43**, 375–394.
58 S. Lu, Q. Li, L. Bai and R. Wang, *Energy Convers. Manage.*, 2019, **197**, 111864.
59 S. Song, X. Xiong, X. Wu and Z. Xue, *Int. J. Hydrogen Energy*, 2021, **46**, 20065–20077.
60 L. Breiman, *Mach. Learn.*, 2001, **45**, 5–32.
61 M. Lazri and S. Ameur, *Atmos. Res.*, 2018, **203**, 118–129.
62 A. M. Shetty, M. F. Aljunid, D. H. Manjaiah and A. M. S. Shaik Afzal, in *Data Science and Applications*, eds. S. J. Nanda, R. P. Yadav, A. H. Gandomi and M. Saraswat, Springer Nature, Singapore, 2024, pp. 451–474.
63 B.-K. Park and S. A. Barnett, *J. Mater. Chem. A*, 2020, **8**, 11626–11631.
64 M. Morales and M. Á. Laguna-Bercero, *ACS Appl. Energy Mater.*, 2018, **1**, 2024–2031.
65 S. Vafaeenezhad, A. R. Hanifi, M. A. Laguna-Bercero, T. H. Etsell and P. Sarkar, *Mater. Futures*, 2022, **1**, 042101.
66 B. Alhijawi and A. Awajan, *Evol. Intell.*, 2024, **17**, 1245–1256.
67 R. Danzer, P. Supancic, J. Pascual and T. Lube, *Eng. Fract. Mech.*, 2007, **74**, 2919–2932.

